Time-dependence of the alpha to epsilon phase transformation in iron

R. F. Smith, J. H. Eggert, D. C. Swift, J. Wang, T. S. Duffy, D. G. Braun, R. E. Rudd, D. B. Reisman, J.-P. Davis, M. D. Knudson, and G. W. Collins

Citation: Journal of Applied Physics **114**, 223507 (2013); doi: 10.1063/1.4839655
View online: http://dx.doi.org/10.1063/1.4839655
View Table of Contents: http://scitation.aip.org/content/aip/journal/jap/114/22?ver=pdfcov
Published by the AIP Publishing

Time-dependence of the alpha to epsilon phase transformation in iron

R. F. Smith,[1] J. H. Eggert,[1] D. C. Swift,[1] J. Wang,[2] T. S. Duffy,[2] D. G. Braun,[1] R. E. Rudd,[1] D. B. Reisman,[1] J.-P. Davis,[3] M. D. Knudson,[3] and G. W. Collins[1]
[1]*Lawrence Livermore National Laboratory, P.O. Box 808, Livermore, California 94550, USA*
[2]*Department of Geosciences, Princeton University, Princeton, New Jersey 08544, USA*
[3]*Sandia National Laboratories, Albuquerque, New Mexico 87185, USA*

(Received 7 October 2013; accepted 12 November 2013; published online 11 December 2013)

Iron was ramp-compressed over timescales of $3 \leq$ t(ns) ≤ 300 to study the time-dependence of the $\alpha \rightarrow \varepsilon$ (bcc→hcp) phase transformation. Onset stresses $(\sigma_{\alpha\rightarrow\varepsilon})$ for the transformation ~14.8-38.4 GPa were determined through laser and magnetic ramp-compression techniques where the transition strain-rate was varied between $10^6 \leq \dot{\mu}_{\alpha\rightarrow\varepsilon}(s^{-1}) \leq 5\times10^8$. We find $\sigma_{\alpha\rightarrow\varepsilon} = 10.8 + 0.55\ \ln(\dot{\mu}_{\alpha\rightarrow\varepsilon})$ for $\dot{\mu}_{\alpha\rightarrow\varepsilon} < 10^6$/s and $\sigma_{\alpha\rightarrow\varepsilon} = 1.15(\dot{\mu}_{\alpha\rightarrow\varepsilon})^{0.18}$ for $\dot{\mu}_{\alpha\rightarrow\varepsilon} > 10^6$/s. This $\dot{\mu}$ response is quite similar to recent results on incipient plasticity in Fe [Smith *et al.*, J. Appl. Phys. **110**, 123515 (2011)] suggesting that under high rate ramp compression the $\alpha \rightarrow \varepsilon$ phase transition and plastic deformation occur through similar mechanisms, e.g., the rate limiting step for $\dot{\mu} > 10^6$/s is due to phonon scattering from defects moving to relieve strain. We show that over-pressurization of equilibrium phase boundaries is a common feature exhibited under high strain-rate compression of many materials encompassing many orders of magnitude of strain-rate. © *2013 AIP Publishing LLC*. [http://dx.doi.org/10.1063/1.4839655]

I. INTRODUCTION

Understanding the nature and time-dependence of material deformation under dynamic loading conditions is an important goal in condensed matter physics. As the interatomic spacing decreases, overlapping electronic band structure and increased levels of stress can fundamentally alter the transport, chemical, and mechanical characteristics of a solid. In Fe, under conditions of near-hydrostatic pressure, as pressure increases, there is a phase transformation from the ambient body-centered-cubic [bcc] α-phase to a hexagonal-closed packed [hcp] ε-phase at 15.3 GPa with an associated 5% volume collapse.[1] A large (shear-stress dependent) hysteresis of the transition is observed with a midpoint pressure of 12.9 GPa.[1] Under the near instantaneous loading associated with uniaxial shock compression, the $\alpha \rightarrow \varepsilon$ phase transformation in polycrystalline Fe samples has also been observed, after a period of stress relaxation, to initiate at 12.9 GPa.[2–4]

Since its discovery, an understanding of the time-dependence and nature of the Fe $\alpha\rightarrow\varepsilon$ phase transformation has been the goal of research across many experimental platforms and time scales.[2–10] Transformation to the $\varepsilon-$phase may be described through a process of nucleation and growth[6,11] where the growth rate is dependent on the flow velocity of martensitic interfaces through the crystal lattice.[12] The rate of plastic accommodation of the new phase is achieved through the movement and generation of martensitic interfacial dislocations.[12] In this paper, we explore how the compressive strain rate $\left(\dot{\mu} = \frac{1}{\rho}\frac{d\rho}{dt}\right)$ affects the onset stress of the $\alpha \rightarrow \varepsilon$ transition in Fe. We use recently developed laser and magnetic ramp-wave-loading (RWL) techniques[13,14] to compress Fe foils with timescales of $3 \leq$ t(ns) ≤ 300. Data show that for $\dot{\mu}_{\alpha\rightarrow\varepsilon} < 10^6$/s, the $\alpha \rightarrow \varepsilon$ onset stress $\sigma_{\alpha\rightarrow\varepsilon} = 10.8 + 0.55\ \ln(\dot{\mu}_{\alpha\rightarrow\varepsilon})$ and for $\dot{\mu}_{\alpha\rightarrow\varepsilon} > 10^6$/s, $\sigma_{\alpha\rightarrow\varepsilon} = 1.15(\dot{\mu}_{\alpha\rightarrow\varepsilon})^{0.18}$. The sudden increase of $\sigma_{\alpha\rightarrow\varepsilon}$ with $\dot{\mu}_{\alpha\rightarrow\varepsilon}$ for $\dot{\mu}_{\alpha\rightarrow\varepsilon} > 10^6\ s^{-1}$ is consistent with the rate of new phase growth being limited at high strain rates by energy dissipation due to phonon scattering from defects moving to relieve strain.[12,33] Over-pressurization beyond equilibrium phase boundaries at high strain rates is not unique to Fe but appears to be a common phenomenon.

This paper is laid out as follows. The experimental methods for three platforms are described in Sec. II. The results are summarized in Sec. III including rate-dependent stress-density response, over-pressurization and a kinetics model that helps understand the trends. There is a discussion of the data in Sec. IV with conclusions in Sec. V.

II. EXPERIMENTAL METHOD

The RWL data were obtained for Fe on the Janus[15] and Omega[16] laser facilities and the Sandia Z-machine.[17,20] The target design employed for the experiments conducted on the Janus laser facility, shown in Fig. 1(a), consists of a 100 μm polyimide [$C_{22}H_{10}N_2O_5$] foil followed by a 150–350 μm vacuum gap and an Fe/sapphire-window target. The polyimide was irradiated for 4 ns by the 1 mm-square spatially planar 527-nm Janus laser (300 J), generating an ablatively driven shock. After shock breakout from the rear surface, the CH rarefies across the vacuum gap, monotonically loads-up against an Fe sample, and launches a temporally-smooth ramp-compression wave.[13] By changing the vacuum gap separation and laser intensity, it is possible to vary the initial maximum compression rate by a factor of ~40. Under these conditions, peak stress states of 15–50 GPa are obtained over several to tens of ns. For these experiments, high purity (99.995%) Fe was deposited in 10–36 μm layers onto a sapphire [001] window under conditions that yielded a grain size of ~5 μm in the stress loading direction and ~1 μm in-plane. The Fe had a strong [110] fiber texture in the growth (pressure loading) direction and was measured to be

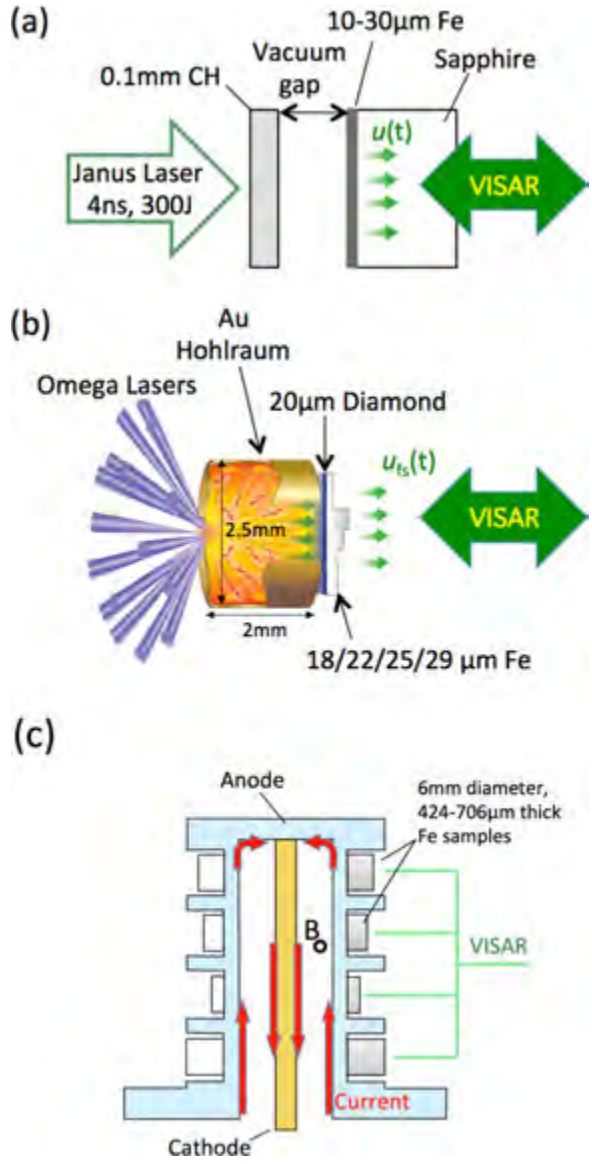

FIG. 1. Target design for (a) Janus laser, (b) Omega laser, and (c) Sandia Z-machine ramp compression experiments.

fully dense (7.87 g/cm^3) to within an accuracy of 0.6%. Sapphire was chosen as a window material as it has a similar mechanical impedance to Fe, thereby minimizing wave reflections at the Fe-sapphire interface.

The target design for the RWL experiments on the Omega laser consists of a stepped iron sample deposited by vapor deposition onto a CVD diamond ablator (20-μm thick, 1.5-mm diameter)[18] yielding the same density and microstructure as used in the Janus experiments. The iron targets had three steps (four thicknesses) that were formed using a mask that was shifted to different positions during the deposition process. The final Fe step thicknesses of 18.10/21.76/25.44/28.67 μm were determined through white light interferometry techniques to within an accuracy of $<$0.1 μm. The target was driven over a 1.5 mm diameter by x-radiation from a Au hohlraum, generating a temporally smooth ramp-compression wave (Fig. 1(b)). The high spatial planarity associated with the x-ray drive from the Omega laser meant different thicknesses of Fe could be compressed with a common compression history to peak stress states of $\sim$270 GPa. Due to the planar, inertially confined nature of the ramp drive, our samples are in a state of uniaxial strain. Here, stress and strain are defined as $\sigma = \sigma_{xx}$ and $d\mu = d\rho/\rho$. A full description of the experimental setup may be found in Ref. 18.

The primary diagnostic for the RWL experiments on the Janus and Omega lasers was the line-imaging velocity interferometer system for any reflector (VISAR), which recorded the velocity history of the Fe/sapphire interface velocity $u_i(t)$ (Janus) or the Fe free-surface velocity, $u_{fs}(t)$ (Omega). The VISAR system has a 1-mm field-of-view, a velocity accuracy of $\sim$50 m/s and a streak camera temporal resolution of $\sim$0.05 ns.[19]

The setup for the Sandia Z experiment set is shown schematically in Fig. 1(c) and is similar to the experiment described in Ref. 17. Current flow through an anode-cathode geometry creates a magnetic drive, which compresses an Fe sample array to pressures of $\sim$300 GPa over 300 ns.[20] Four samples of Fe (99.995% pure, OD = 6 mm) with 423.62/531.74/600.24/705.99 μm thickness were glued to the Cu anode. Cu was used for impedance matching of the samples to minimize wave interaction and release effects. The sample disks were lapped to the desired thickness and coated with 0.3 μm Al to enhance reflectivity and prevent oxidation. During ramp-compression the free-surface velocity history of each Fe sample was recorded using a point VISAR.[21] Two fiber-optic bundles, one at the center and one vertically offset by 1.5 mm along each sample, collected the VISAR signal. $u_{fs}(t)$ was measured on each sample with 2–5 independent VISAR channels and up to four different sensitivities (0.2962 to 0.848 km/s per fringe). The characteristic ramp compression rise time is up to one hundred times slower for magnetic loading using Z than for laser-based loading at the Janus or Omega laser facilities.

III. RESULTS

A. Determination of α→ε onset stress

The $u_{fs}(x,t)$ data obtained on the Sandia Z-machine and the Omega laser are shown in Figs. 2(a) and 2(b), respectively. In both cases, a common pressure load was applied to all step thicknesses with characteristic compression strain-rates of $\sim 10^6\,s^{-1}$ (Z) and $\sim 10^8\,s^{-1}$ (Omega); estimated directly from the $u_{fs}(t)$ profiles and the determined stress-density response, as discussed below. Two independent VISAR measurements are shown for each step thickness (blue and black curves). The velocity range and analysis considered here are limited to the low compression portion of the profiles. In RWL experiments, analysis of free surface velocity histories from multiple thickness samples can yield continuous information on the bulk properties of Lagrangian sound speed (C_L), stress (σ_x), density (ρ), and particle velocity (u).[17,18,22] This is achieved through an iterative characteristics-based Lagrangian sound speed analysis technique which corrects for wave interactions at the free surface.[23] Shown in Fig. 3 are the extracted $C_L(u_{fs}, \rho)$ and $\sigma_x - \rho$ relationships for Z shot z1682 (blue curve) and Omega shot s58588 (red curve). $C_L(u_{fs}, \rho)$ represents an average value measured across the distance from the

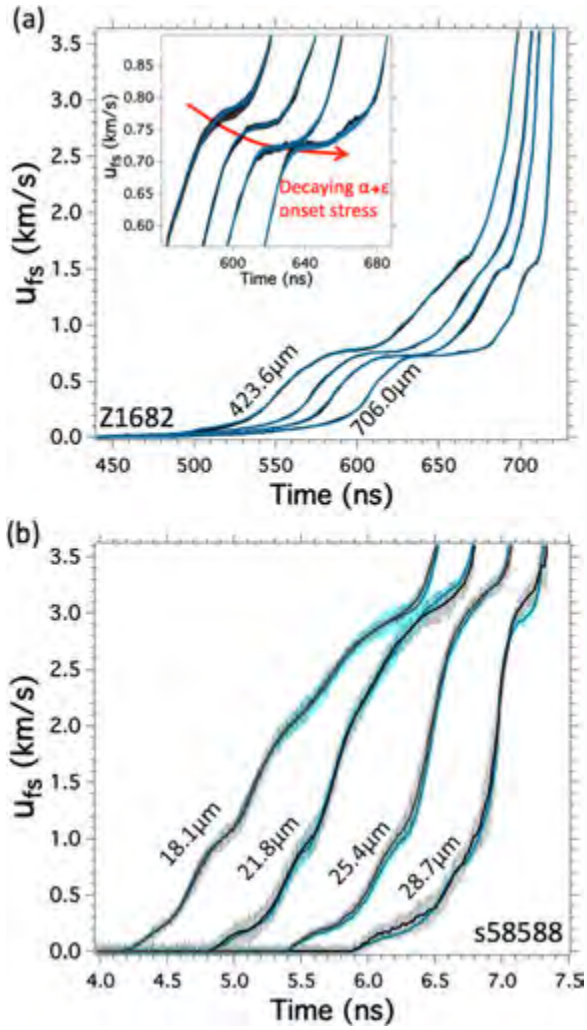

FIG. 2. Free-surface velocity versus time traces from RWL experiments on (a) the Sandia Z-machine (shot no. z1682) and (b) the Omega laser (shot no. s58588). The inset of (a) shows the time-dependent decay of the velocity plateau associated with the $\alpha \rightarrow \varepsilon$ phase transformation.

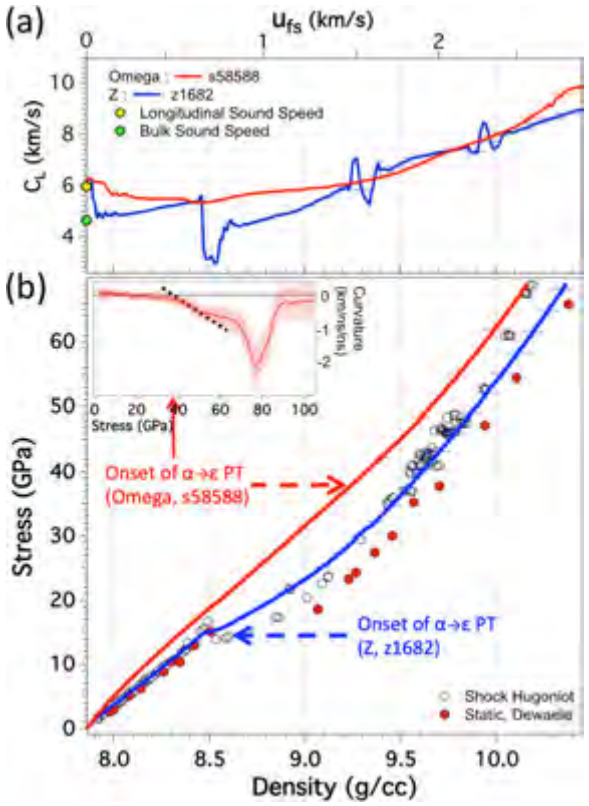

FIG. 3. (a) Lagrangian Sound Speed (C_L) as a function of u_{fs} and density for Z shot z1682 (blue curve) and Omega shot s58588 (red curve) determined from Lagrangian sound speed analysis of the u_{fs}(t) profiles shown in Fig. 2. The longitudinal and bulk sound speeds are labeled as yellow and green solid circles, respectively.[18] (b) Stress-density is plotted with previous shock[24–28] and static compression[29] data on Fe. The onset of time-dependent compression in the Omega data is identified by a curvature analysis that determines the stress at which the wave velocity varies in time (see text for details). The estimated stress onset for the $\alpha \rightarrow \varepsilon$ phase transformation is 14.8 GPa for the low strain-rate Z data and 38.4 GPa for the high strain-rate Omega data (s58588).

thinner sample to the thicker sample as determined from a fit through breakout time versus sample thickness. Any variation in rate-dependent material response over this distance, with a resultant change in the sound speed, compromises the simple wave assumptions of the Lagrangian analysis in determining the $\sigma_x - \rho$ response.

In the Z u_{fs}(t) data (Fig. 2(a)), we observe a velocity plateau at $u_{fs} \sim 0.75$ km/s attributable to a drop in C_L and consistent with the onset of the $\alpha \rightarrow \varepsilon$ phase transformation (Fig. 3(a)).[3,8] A decay in the velocity of this plateau as a function of time, symptomatic of the time-dependence associated with the phase transformation, is shown as Fig. 2(a) inset. Further ramped plateaus are observed in the velocity traces at ~1.5 km/s and (less obviously) at ~2.3 km/s. Both characteristics and hydrodynamic simulations, which model the wave propagation through the sample, determine that these features result from the phase transformation velocity plateau reflection off the free surface interacting with the oncoming ramp.[3] As both of these plateaus decay with propagation distance, the average C_L in Fig. 3(a) exhibits an oscillation at these u_{fs} values. For the high strain rate Omega data, no velocity plateau (Fig. 2(b)) or abrupt drop in $C_L(u_{fs})$ (Fig. 3(a)) associated with the phase transformation is observed. The ramped plateau observed at $u_{fs} \sim 3$ km/s is due to temporal variation within the initial ramp compression load common to all thicknesses caused by an emerging elastic wave from the diamond ablator.[18]

In Fig. 3(b), the calculated stress-density response is shown along with previous shock[24–28] and static compression data[29] on Fe. For the Z data (blue curve), there is a clear kink in the stress-density profile at ~14.8 GPa, which is a signature of transformation into the denser ε phase. This is an average value based on analysis of all the u_{fs}(t) profiles shown in Fig. 2(a). We note that the Z data, which has a characteristic strain-rate of $\sim 10^6\,s^{-1}$, follows a similar stress-density path to the quasi-static data of Dewaele[29] and the low strain-rate shock compression data. By contrast, the high strain-rate ($\sim 10^8\,s^{-1}$) Omega laser data exhibit no clear change in slope within stress-density (red curves) that would be a signature of the ε-phase onset even though it has previously been established in laser shock-driven x-ray diffraction experiments that this phase transformation does occur over these rapid compression timescales.[7,10] We note that the lower compressibility of the Omega data below 12.9 GPa is due to the material strength, which increases dramatically at

these high strain rates.[33] Above this pressure, the lower compressibility is expected to be a function of both the material strength and the kinetics of the phase transformation.

For RWL, where the rate of compression increases as a function of time, the onset of rate-dependent material response due to the phase transformation causes $C_L(u)$ to vary with sample thickness. This rate-dependent material response is captured within the *curvature* variable defined from a quadratic fit to step thickness versus breakout time as a function of stress (inset of Fig. 3(b)). Essentially, C_L reported in Fig. 3(a) can be thought of as an average wave speed over Δx and a curvature in C_L denotes a change in the average wave speed, and thus departure from simple wave behavior, and an onset of rate-dependence. The departure from *curvature* = 0 represents a change in $C_L(u)$ with sample thickness consistent with the onset of a variable time-dependent material response associated with $\sigma_{\alpha\to\varepsilon}$; here defined as the stress at the intersection of negative *curvature* slope (dashed black line in Fig. 3(b) inset) with the *curvature* = 0 contour. At higher stresses, a convergence towards *curvature* of 0 is expected upon completion of time-dependent transformation into the ε-phase. Our analysis is consistent with $\sigma_{\alpha\to\varepsilon}$ values of 38.4 GPa for the high strain-rate Omega data (s58588) and 14.8 GPa for the low strain-rate Z data (shot z1682); values significantly above the 12.9 GPa equilibrium phase transformation stress.[1–4]

Stress as a function of time and Lagrangian position for Omega shot s58588, $\sigma_x(x,t)$, as calculated from the iterative Lagrangian sound speed analysis, is shown in Fig. 4(a). The free surface is at zero pressure, and so the phase transformation front is always within the bulk of the sample and not directly observable with the VISAR. The contour for the estimated $\sigma_{\alpha\to\varepsilon}$ of 38.4 GPa is shown as the yellow dashed curve. The inset highlights the complicated wave interactions which occur close to the rear surface where an element of material can experience a rapid increase and decrease in stress relative to the critical phase transformation stress over sub-ns timescales.

Fig. 4(b) shows the calculated strain rate ($\dot{\mu} = \frac{1}{\rho}\frac{d\rho}{dt}$) versus time and Lagrangian position for Omega shot s58588. The x, t of the $\sigma_{\alpha\to\varepsilon} = 38.4$ GPa contour from Fig. 4(a) is also shown. Lineouts of $\dot{\mu}(t)$ along the path of the 38.4 GPa contour are shown in Fig. 4(c) for all the step thicknesses. At times after the initial arrival of the 38.4 GPa contour near the free surface ($t \sim 7$ ns), there is a negative strain rate due to the wave reflections from the free-surface. These regions of negative strain rate (shown as dashed curves) have been multiplied by −1 in order to be represented on the plot. Over the whole Fe sample, there is an increase in strain rate from $10^8\ s^{-1}$ at the initial compression surface to a maximum of $\sim 6\times10^8\ s^{-1}$ associated with the initial arrival of the 38.4 GPa characteristic near the free-surface (6.7 ns for the 28.7 μm step). This peak strain-rate is reduced for thinner steps with the maximum value for the 18.2 μm step $\sim 1.8\times10^8\ s^{-1}$ ($t \sim 4.7$ ns). From this analysis, we define an average longitudinal strain-rate associated with $\sigma_{\alpha\to\varepsilon} \sim 38.4$ GPa as $\dot{\mu}_{\alpha\to\varepsilon} \sim 3\times10^8\ s^{-1}$. Similar analysis on the Z shot z1682 gives an average strain rate of $3\times10^6\ s^{-1}$ associated with $\sigma_{\alpha\to\varepsilon}$ of 14.8 GPa. These values are well approximated by

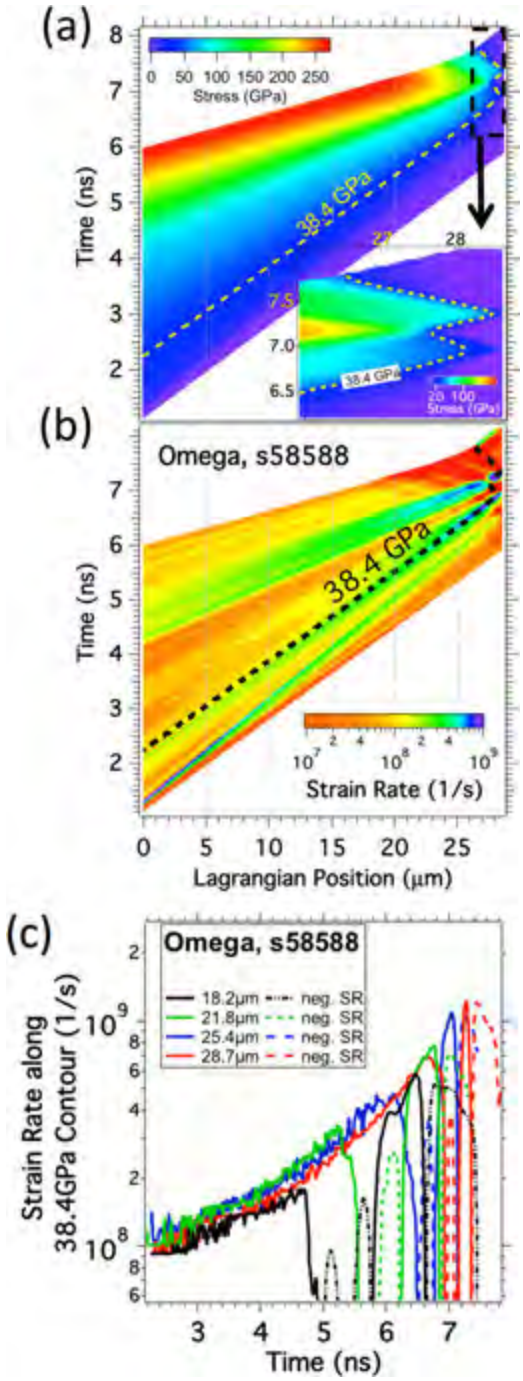

FIG. 4. (a) Stress as a function of time and Lagrangian position for Omega shot s58588 as calculated from u_{fs}(t) profiles in Fig. 2(b) and an iterative Lagrangian sound speed analysis. The determined $\sigma_{\alpha\to\varepsilon} = 38.4$ GPa contour is shown as the yellow dashed curve. Inset figure highlights complicated wave interactions near the free-surface. (b) Calculated strain rate as function time and position. (c) Strain rate as a function of time along $\sigma_{\alpha\to\varepsilon} = 38.4$ GPa contour for each step thickness. Negative strain rates have been multiplied by −1 in order to appear on the same scale (dashed curves).

defining[30] a characteristic longitudinal strain-rate associated with the $\alpha \to \varepsilon$ transformation directly from the u_{fs}(t) data

$$\dot{\mu}_{\alpha\to\varepsilon} = \frac{\rho}{\rho_0}\frac{du/dt}{C_L}, \tag{1}$$

where $u \approx u_{fs}/2$. du/dt and C_L are taken at the transition stress described above.

We note that rapid variation of $\dot{\mu}$ and σ near the free-surface can generate complicated time-dependent material response associated with the evolving phase front. This behavior is not captured by the iterative Lagrangian analysis technique and can affect the stress-density determination. A recent study[18] on Fe, in which the compression rate through the $\alpha \rightarrow \varepsilon$ phase transformation was varied from 10^8 to $10^9\,s^{-1}$, showed that for compression within the high-pressure epsilon phase the determined $\sigma_x - \rho$ response was not strongly affected by the rate dependence of the $\alpha \rightarrow \varepsilon$ phase transformation.

B. Over-pressurization of equilibrium phase transformation stress

A typical $u_i(t)$ profile for a ramp-loaded polycrystalline Fe sample recorded on the Janus laser is shown in Fig. 5. A three-wave structure emerges at the Fe/sapphire interface: an elastic wave with a peak velocity of u_E, a plastic wave P1 with a peak velocity $u_{\alpha\rightarrow\varepsilon}$, which is followed by a pronounced velocity pullback after the peak, and a subsequent plastic wave P2. This transformation from the smoothly rising load profile to the structured transmitted-wave profile is understood by considering the target dynamics in Lagrangian coordinates as discussed in Ref. 13. The initial one-dimensional elastic deformation is characterized by stress propagation at the longitudinal sound speed. Immediately behind the elastic front, where deformation is dominated by plasticity, stress waves propagate at the lower bulk sound speed, which results in wave separation as a function of time. For stress levels above 12.9 GPa, the $\alpha\rightarrow\varepsilon$ structural phase transformation may initiate causing a drop in the Lagrangian sound speed as the material evolves into the new ε-phase. Due to the time-dependence associated with the transformation, there is a rapid velocity pullback in the $u_i(t)$ record at that transition related to stress relaxation caused by an evolving volume collapse into the denser hcp phase.[6] Due to the slightly higher impedance of sapphire, and unlike the free-surface samples, the VISAR is directly observing the phase transformation wave.[13] $\dot{\mu}_{\alpha\rightarrow\varepsilon}$ is defined over the velocity interval $u_{\alpha\rightarrow\varepsilon}$ to the minimum pull-back velocity (Fig. 5 and Eq. (1)).

In Fig. 6(a), we plot the $\sigma_{\alpha\rightarrow\varepsilon}$ for polycrystalline Fe as a function of target thickness for the Janus, Omega, and Z ramp data. In addition to the data already discussed, we include in this analysis free-surface measurements obtained with a gas-gun driver[3,5] and those determined from reported Fe/sapphire $u_i(t)$ profiles from the Sandia Z-machine.[6,31] The circle and square symbols represent data for ramp and shock loading, respectively. The velocity of the Fe/sapphire interface for the Janus, Jensen[31] and Bastea[6] data was converted to an equivalent longitudinal stress and particle velocity, u, within the bulk Fe using standard impedance matching

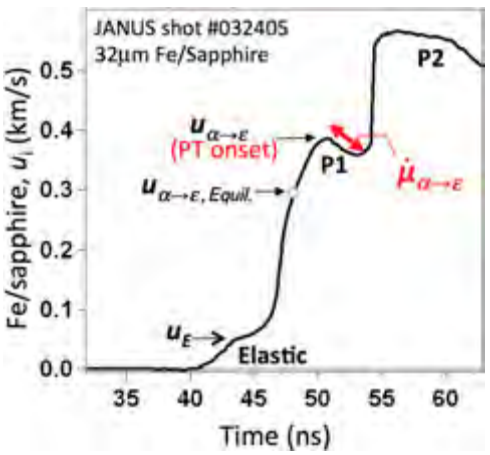

FIG. 5. Fe/sapphire particle velocity versus time for Janus laser-driven ramp compression of an Fe foil (spatially averaged over ~1-mm diagnostic field-of-view). The VISAR records the emergence of a three wave structure at the Fe/sapphire interface: an elastic wave, a plastic wave (P1) with a peak stress associated with the onset of the $\alpha \rightarrow \varepsilon$ phase transformation and a subsequent plastic wave (P2) within which transformation to the epsilon-phase occurs. $\dot{\mu}_{\alpha\rightarrow\varepsilon}$ is the strain-rate associated with the transformation into the ε-phase and is found to be strongly correlated to the phase transformation onset velocity, $u_{\alpha\rightarrow\varepsilon}$. $u_{\alpha\rightarrow\varepsilon,\,Equil.}$ represents the interface velocity equivalent to the 12.9 GPa equilibrium phase transformation stress. At these high strain-rates equilibrium phase boundaries are strongly over-pressurized.

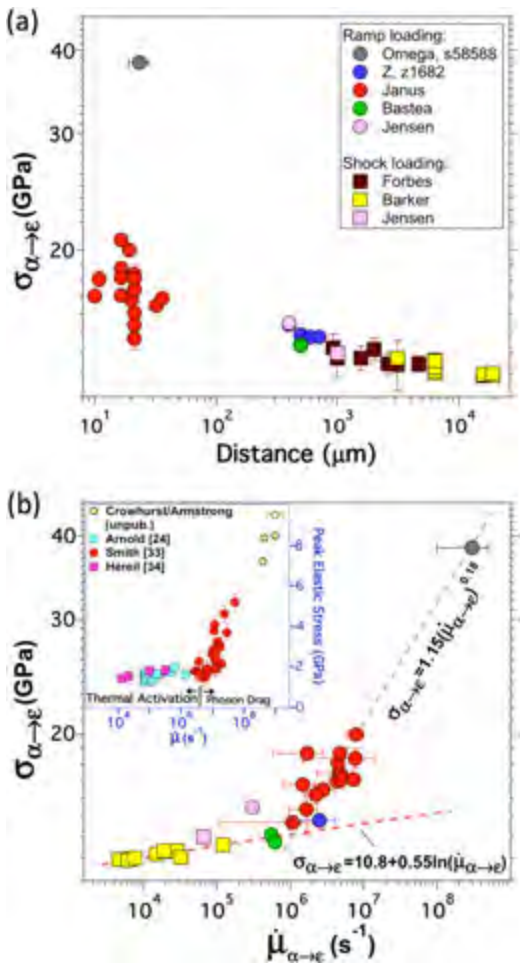

FIG. 6. (a) Stress associated with initiation of $\alpha\rightarrow\varepsilon$ phase transformation, $\sigma_{\alpha\rightarrow\varepsilon}$, as a function of propagation distance from the loading surface. (b) $\sigma_{\alpha\rightarrow\varepsilon}$ as a function of strain-rate associated with the phase transition, $\dot{\mu}_{\alpha\rightarrow\varepsilon}$. We observe a strong increase in $\sigma_{\alpha\rightarrow\varepsilon}$ for $\dot{\mu}_{\alpha\rightarrow\varepsilon} > \sim 10^6\,s^{-1}$. Inset Fig: Peak elastic stress versus strain-rate at the onset of plastic flow in Fe (reproduced from Ref. 33). The unpublished data of Crowhurst and Armstrong was obtained on shock compression of ~1 μm thick Fe samples using experimental techniques described in Ref. 35. The sudden increase of elastic and phase transformation onset stresses at strain-rates $>\sim 10^6\,s^{-1}$ is consistent with an expected transition to a high strain-rate phonon drag regime where dislocation velocities become limited by energy dispersion from lattice vibrations.

techniques. We assume an elastic equation-of-state (EOS) for sapphire[32] and an EOS for Fe determined from Omega multi-stepped data in Fig. 3(b) and summarized in Ref. 18. The error bars on the Janus data take into account the inherent accuracy of the (VISAR) measurement and uncertainties due to drive non-uniformity. The errors for the Omega data reflect the uncertainty in sample thickness and in determining the onset stress of time-dependent deformation associated with the phase transformation (Sec. III A). There is a general trend of $\sigma_{\alpha\to\varepsilon}$ decay towards an equilibrium value at late times (thick samples) since for both shock and ramp loading, time-dependent plastic flow behind the phase transformation front causes the phase transformation onset stress, $\sigma_{\alpha\to\varepsilon}$, to decay as a function of propagation distance.[33] After $\sim$20 mm of propagation ($>3\,\mu$s propagation time) $\sigma_{\alpha\to\varepsilon} = 12.9$ GPa.[3] For RWL, the stress associated with the onset of time-dependent deformation processes, such as an elastic-to-plastic transition or a phase transformation, has a unique relationship with the compression wave rise time.[33] The high degree of scatter for the 10–30 μm thick samples in Fig. 6(a) is due to the large range of associated ramp compression rates.

In Fig. 6(b), we plot the phase transformation onset stress as a function of transition strain-rate and find an improved correlation, with $\sigma_{\alpha\to\varepsilon}$ increasing as a function of $\dot{\mu}_{\alpha\to\varepsilon}$. The strain rate values associated with the Jensen[31] and Bastea[6] Fe/sapphire data were calculated directly from the reported $u_i(t)$ profiles. $\dot{\mu}_{\alpha\to\varepsilon}$ from the free-surface data of Barker[3] was determined from the reported maximum P2 velocity slope (du_{fs}/dt) combined with Eq. (1) and assuming $u \approx u_{fs}/2$. The data in Fig. 6(b) reveal a relative insensitivity of $\sigma_{\alpha\to\varepsilon}$ with ε-phase transition strain rate in the range of $\sim 10^3$–$10^6\,s^{-1}$. At $\dot{\mu}_{\alpha\to\varepsilon} > \sim 10^6\,s^{-1}$, there is a marked increase in $\sigma_{\alpha\to\varepsilon}$ scaling with $\dot{\mu}_{\alpha\to\varepsilon}$.

The data in Fig. 6 represent the instantaneous value for $\sigma_{\alpha\to\varepsilon}$ after propagation through a range of Fe sample thicknesses; a data set which encompasses a wide range of loading rates. A quantitative description of $\sigma_{\alpha\to\varepsilon} - \dot{\mu}_{\alpha\to\varepsilon}$ material response at a distance x′ from the loading surface is highly complex and is a convolution of the instantaneous material response and the integrated time-dependent response from $x = 0 \to x'$. Under dynamic loading conditions, and due to time-dependent material response, $\sigma_{\alpha\to\varepsilon}$ and $\dot{\mu}_{\alpha\to\varepsilon}$ decrease in time from peak values at the initial compression or loading surface ($x = 0$) to equilibrium values at late time. In recent work on Fe and Al,[33] we found that, independent of sample thickness, there exists a strong correlation between *instantaneous* values of the peak elastic stress, σ_E, and the strain-rate at the onset of plastic flow, $\dot{\mu}_p$. For $\dot{\mu}_p > \sim 5 \times 10^6\,s^{-1}$, σ_E increases sharply with $\dot{\mu}_p$ (inset of Fig. 6(b); figure[24,33,34] adapted from Ref. 33). That the $\dot{\mu}$ response in Fig. 6(b) is quite similar to recent results on incipient plasticity in Fe suggests that the $\alpha \to \varepsilon$ phase transition and the transformation to mostly plastic deformation occur through similar mechanisms.

A number of phenomenological constitutive models have been developed to describe the $\sigma - \dot{\mu}$ relationship in bcc metals associated with plasticity.[36] A general form of these models predicts a $\sigma \propto \ln(\dot{\mu})$ dependency in the thermally activated dislocation flow regime with a transition to a $\sigma \propto (\dot{\mu})^n$ high strain-rate response where dislocation velocities become limited through energy dissipation off phonon modes within the sample (phonon drag). $n < 1$ suggests an increase in saturation dislocation density with increasing strain-rate.[37] In our data, we observe two distinct strain-rate regimes. A fit to the low strain-rate data, shown as the dashed red curve in Fig. 6(b) is represented by

$$\sigma_{\alpha\to\varepsilon} = 10.8 + 0.55\ln(\dot{\mu}_{\alpha\to\varepsilon}), \tag{2}$$

which is consistent with thermally activated dislocation flow facilitating the plastic accommodation of the emerging hcp phase within the bcc lattice (see Discussion section). For $\dot{\mu}_{\alpha\to\varepsilon} > \sim 10^6\,s^{-1}$, $\sigma_{\alpha\to\varepsilon}$ increases sharply with $\dot{\mu}_{\alpha\to\varepsilon}$. This sudden change in material response is consistent with the onset of phonon drag at high dislocation velocity.[36] A fit to the high strain-rate data, shown as the dashed grey curve in Fig. 6(b), is represented by

$$\sigma_{\alpha\to\varepsilon} = 1.15\dot{\mu}_{\alpha\to\varepsilon}{}^{0.18}. \tag{3}$$

The data in Fig. 6(b) are consistent with a change in the dislocation flow mechanism from thermal activation to phonon drag at $\sigma_{\alpha\to\varepsilon} \sim 14$ GPa and $\dot{\mu}_{\alpha\to\varepsilon} \sim 1 \times 10^6\,s^{-1}$. This transition strain rate is $\sim 5\times$ less that the equivalent transition strain rate change identified for incipient plasticity (inset to Fig. 6(b)). The martensitic interface dislocations that govern ε-phase growth are not the same as the bulk screw dislocations that govern plasticity. While they are expected to undergo an activation to drag transition, it would be expected to happen at a different strain rate.

We note that the measured strain rates in the shock compression experiments are lower than for the RWL experiments. Shock compression experiments are characterized by a fixed high strain-rate ($\sim 10^9\,s^{-1}$) at the loading surface, which decreases as a function of propagation distance due to dissipative processes within the material such as strength, viscosity, and heat conduction.[38] Traditional methods of measuring high-strain-rate material response on gas guns use $\sim$mm thick samples and are limited to peak measured strain-rates of $< \sim 10^6\,s^{-1}$.[33] Under shock compression, wave profile analysis has been used to infer $\alpha \to \varepsilon$ transformation times of 50–180 ns,[3] <50 ns,[5] 12-60 ns,[8] and <1 ns to 200 ns.[4] This variation in the reported $\alpha \to \varepsilon$ completion time is due in large part to the range of experimental conditions employed (peak shock stress, sample thicknesses) to measure a transition rate which evolves rapidly in time and space under dynamic compression conditions.

C. Phase transformation kinetics model

To investigate the experimental trends, ramp compression in Fe was simulated over a wide range of strain rates with a multiphase EOS model incorporating explicit phase transition kinetics. Each phase was described by a thermodynamically complete, analytic EOS, following a prescription developed for MgO.[39] The EOS parameters were adjusted to reproduce pure-phase regions of a tabular multiphase EOS.[40] At each location in the sample, the material was taken to comprise a mixture of phases, each with its own thermodynamic state. A kinetics model was used to describe the rate of

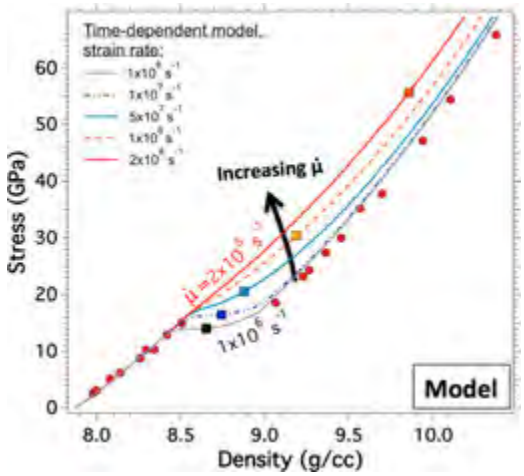

FIG. 7. A time-dependent phase-transition model shows the stress-density response of Fe as a function of ramp strain rate (see text for details). The solid squares on each curve represent the stress for a predicted 50% ε-phase population within the sample. The red hexagonal symbols represent the quasi-static data of Dewaele.[29]

conversion of the material between phases. The kinetics of the phase transition was treated as a function of the difference in free energy between the candidate phases. Strain rate is calculated directly from the rate applied to a small element of material, without treating the response of a finite sample by wave propagation. Once the ramp compression rate becomes comparable to the transformation time (as specified within the model), then the phase transformation becomes over-pressurized. At high levels of over-pressurization, the transition rate is capped consistent with an expected drag behavior. The contribution of the elastic strain state can be included in this formalism, though strength was neglected in this initial study. A full description of the model and the parameters used in the simulations may be found in the Appendix.

Using this model, we plot the predicted stress-density response of Fe as a function of ramp strain rate, as shown in Fig. 7. Also shown for comparison are the static data of Dewaele.[29] On each stress-density curve the square symbol represents the stress state at which there is a 50% population of the new ε-phase. The model predictions are in good agreement with the trends observed in the experimental data in Fig. 3(b). At the very high strain rates associated with laser ramp compression the $\alpha \rightarrow \varepsilon$ phase transformation is strongly over-pressurized.

The data presented in this section suggest that the ability to identify high-pressure phase transformations from wave profile analysis alone may be confounded at high strain rates by the kinetics of the transition coupled with the rapid compression timescales. In such cases, alternative diagnostic approaches, such as x-ray diffraction, would be needed to confirm the existence of a new high-pressure phase.[41] Our data show the importance of considering time-dependent material response when comparing high-strain experimental data with equilibrium models.

IV. DISCUSSION

The $\alpha - \varepsilon$ transformation is understood to be diffusionless and martensitic based on previous experiments and theory,[42,43] and the rapid transformation kinetics reported here are consistent with this picture. Classical nucleation theory (CNT) describes the dynamics of these transitions through a two-stage process: initial slow transformation (nucleation) followed by a rapid growth regime in which the transforming martensitic interface can flow with velocities approaching the local speed of sound.

A phase transformation is possible if the daughter phase has a lower free energy than the parent phase at a given density and temperature.[11,12,48] In Fe, this is assumed to occur under dynamic loading for compressive stresses above the 12.9 GPa equilibrium transition stress. Under these conditions, the lower free energy of the ε-phase favors nucleation, but there is an energy cost associated with the formation of an inter-phase interface. The driving force for nucleus growth scales with the volume of the nucleus while the opposing force, associated with the surface tension of a newly formed interface, scales with the surface area.[11,44] There is a critical nucleus volume, V_0, where the driving forces are sufficient to overcome the back stress and spontaneous growth can ensue. The initial growth rate is slow and depends on the ability of the parent phase to plastically accommodate the growth of the new phase where the strain field around the nucleus is associated with a network of interacting dislocation loops which need to move through the lattice for growth to occur.[12] After a period of slow growth, the nucleus reaches a critical volume, V*, where the driving forces are sufficient to generate new dislocation loops and rapid growth ensues.

This CNT picture of a two-stage growth into the new phase is now supported by recent experimental observations. Techniques employing neutron[45] and laser light[46] scattering have allowed for the new phase nucleus volume to be measured at discrete times during its evolution allowing researchers to determine the kinetics of the phase transformation in systems where the transformations occurred over several hours. Measurements of new phase nucleation and growth in colloidal systems[46] are consistent with a two-stage process with limited nucleation at early times prior to the onset of rapid growth. Observations of a stress-dependent incubation period (interpreted as the nucleation phase) before the onset of new phase rapid growth has been observed in high strain-rate compression experiments on CdS,[48] Y,[47] and Ti.[47] In the CdS work of Knudson,[48] a phenomenological model based on CNT and modified to incorporate the experimentally observed incubation period dependence on equilibrium over-pressurization was developed. Recent shock data from Jensen[4] on polycrystalline Fe shows that for 1.7 GPa shock over-pressurization, there is an initial incubation period of ~50 ns before rapid transformation into the ε-phase [Fig. 4 in Ref. 4], consistent with expected nucleation and growth behavior.

Figure 8 represents our interpretation of the nucleation and growth time-dependence in the context of our Janus Fe data. Here, the velocity history of the Fe/sapphire interface, $u_i(t)$, is magnified from Fig. 5 to show the detail of particle velocity signatures associated the α (bcc) to ε (hcp) phase transition. The red dashed line represents the 12.9 GPa transformation equilibrium surface in particle velocity space. For higher levels of compression, conditions are favorable for

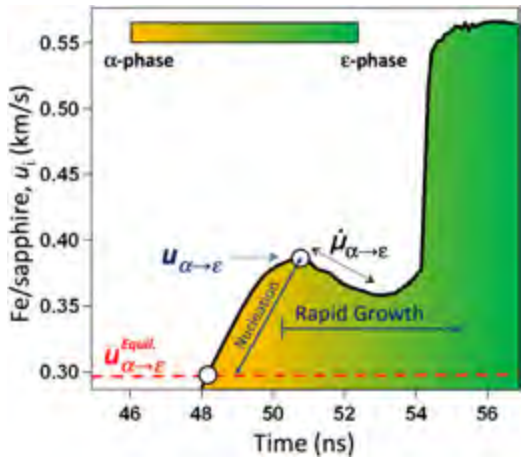

FIG. 8. Interpretation of Fe/sapphire interface velocity profiles from the Janus experiment based on a phenomenological picture of ε−phase nucleation and growth.

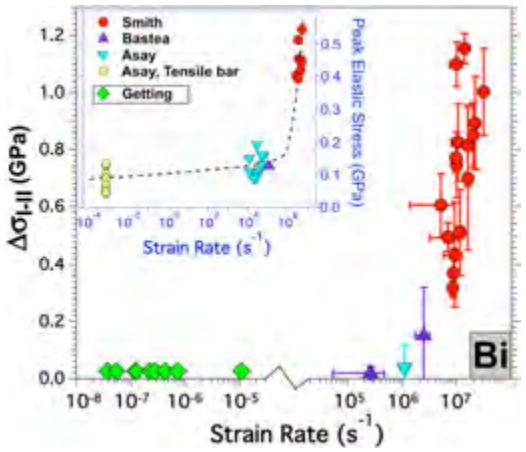

FIG. 9. A strong strain-rate dependence is observed in the over-stress of the Bi I-II phase transformation and the peak elastic stress [inset] (data reproduced from Ref. 13). These data are similar to our observations in Fe (Fig. 6(b)) and are consistent with phonon drag effects altering the deformation response at high strain rates.

nucleation into the ε hcp phase. Once growth of an hcp-nucleus reaches the critical volume, V*, the driving forces are sufficient to generate new dislocation loops and rapid growth of the ε-phase ensues. Stress overpressurization ($\Delta\sigma_{\text{Equil}} = \sigma_{\alpha\to\varepsilon}$ - $\sigma_{\alpha\to\varepsilon,\,\text{Equil}}$) is a driving force determining the rate of rapid growth into the ε-phase ($\propto \dot{\mu}_{\alpha\to\varepsilon}$). This has been verified in Fe by recent shock compression data from Jensen[4] in which the $\alpha \to \varepsilon$ transformation time varied from 200 to <1 ns for initial $\Delta\sigma_{\text{Equil}}$ of 1.69 and 6.54 GPa, respectively. Our data in Fig. 6(b) within the $\sim 10^3$–$10^6\,s^{-1}$ range of strain rate show a weak $\dot{\mu}_{\alpha\to\varepsilon}$ - $\Delta\sigma_{\text{Equil}}$ dependence. However, to facilitate high strain rate deformation into the ε-phase ($\dot{\mu}_{\alpha\to\varepsilon} > \sim 10^6\,s^{-1}$), sharply increased levels of $\Delta\sigma_{\text{Equil}}$ are required (increased free energy difference between parent and daughter phase to drive the transition). At low compression rates, martensitic interfacial dislocation flow can be modeled through thermal activation of dislocations over barriers within the system;[12,48] however, the high $\dot{\mu}$ data in Fig. 6(b) is consistent with a different regime where new-phase nucleus growth within the lattice is limited by phonon drag mediated dislocation velocity.

In our experiments, we observe a pronounced pull-back feature on Fe/sapphire targets recorded *u(t)* trace (at $u_{\alpha\to\varepsilon}$), which is consistent with a drop in the sound speed associated with the rapid growth of the ε-phase. The ~200 ns ramp compression experiments of Bastea[6] on ~500 μm thick Fe/sapphire samples also exhibited a velocity pullback. A nucleation and growth model combined with hydrodynamic simulations applied to those data showed that this velocity pull-back feature is consistent with an evolving volume collapse into the higher density ε-phase under conditions of increasing applied stress.[6] Phenomenological models based on CNT have been successfully applied to describe time-dependent behavior associated with martensitic transformations in Fe,[6] Bi,[49] and CdS[48] under ramp and shock loading.

The similarity in strain rate response for incipient plasticity and the onset of the $\alpha \to \varepsilon$ phase transformation (Fig. 6(b)) suggests similar underlying mechanisms, e.g., the rate limiting step for $\dot{\mu} > 10^6\,s^{-1}$ is due to phonon scattering of strain relieving defects. In the CdS work of Knudson,[48] a significant difference in incubation time (nucleation phase) with crystal orientation was observed, which was suggested to be due to the different yield behavior exhibited by the two orientations. That interpretation is very consistent with the discussion here—the elastic plastic response can strongly influence the nucleation and growth of phase transitions in dynamic experiments. In the experiments of Knudson,[48] it is due to crystal orientation whereas in the data reported here on Fe it is due to a transition from thermal activation to phonon drag.

A number of recent experimental observations over several materials have shown that high-strain rate overpressurization of equilibrium surfaces is general behavior for many materials due to the competing time-scales of material response and applied compression rate.[4,6,22,47–49] Dynamic compression of Bi shows, similar to Fe, a high strain-rate increase in both the peak elastic stress and the Bi I-II phase transformation onset stress (Fig. 9). For strain rates 10^{-8}–$10^5\,s^{-1}$, there is no dependence of the Bi I-II onset stress with strain rate. It is only for $\dot{\mu} > 5 \times 10^6\,s^{-1}$ that the Bi I-II phase transformation onset pressure significantly deviates from equilibrium (see Ref. 13 and references within). These data on the strain-rate dependence of elastic and phase transformation stresses in Bi, combined with similar measurements on Fe, suggest that phonon drag mechanisms may be limiting the growth of the new phase in these materials at $\dot{\mu} > \sim 10^6$–$10^7\,s^{-1}$.

V. CONCLUSIONS

In this paper, we present data from three different experimental platforms in which Fe samples were compressed in the $\sim 10^6$–$10^8\,s^{-1}$ strain-rate range. We show that deformation in Fe is dramatically altered at high strain-rates due to the onset of strong time-dependence in the $\alpha \to \varepsilon$ structural phase transformation. Our data, combined with data from other dynamic compression platforms, reveal a strong correlation between the instantaneous values of the $\alpha \to \varepsilon$ onset stress, $\sigma_{\alpha\to\varepsilon}$, and the transition strain-rate, $\dot{\mu}_{\alpha\to\varepsilon}$. The sudden

increase of $\sigma_{\alpha\to\varepsilon}$ with $\dot{\mu}_{\alpha\to\varepsilon}$ for $\dot{\mu}_{\alpha\to\varepsilon} > 10^6\,\mathrm{s}^{-1}$ is consistent with the rate of new phase growth being limited at high strain-rates by energy dissipation of martensitic interfacial dislocations emitting or scattering off phonon modes within the lattice (phonon drag). We show that over-pressurization of equilibrium phase boundaries is a common feature exhibited under high strain-rate compression of many materials encompassing many orders of magnitude of strain-rate.

ACKNOWLEDGMENTS

This work was performed under the auspices of the U.S. Dept. of Energy by Lawrence Livermore National Laboratory under Contract DE-AC52-07NA27344. The research was supported by NNSA/DOE through the National Laser Users Facility Program under contracts DE-NA0000856 and DE-FG52-09NA29037.

APPENDIX: MULTIPHASE EOS PHASE TRANSFORMATION KINETICS MODEL

The experimental measurements were compared with a multiphase EOS model with explicit phase transition kinetics. Each phase was described by a thermodynamically complete, analytic EOS, following a prescription demonstrated recently for MgO.[39] The pressure p in each single phase was expressed in a Grüneisen form as a function of mass density ρ and specific internal energy e

$$p(\rho, e) = p_k(\rho) + \rho\Gamma(\rho)[e - e_k(\rho)]. \tag{A1}$$

The reference curve $\{p_k,e_k\}(\rho)$ was the zero-Kelvin isotherm (cold curve), represented here by a functional form suggested by Heuzé,[50–53] which is convenient for algebraic inversion

$$p_k(\rho) = \frac{K_0}{N_0+1}[e^{(N_0+1)(1-\rho_0/\rho)} - 1], \tag{A2}$$

where ρ_0, K_0, and N_0 are parameters defining the zero-pressure values of density, bulk modulus, and its volume derivative, respectively. This function can be integrated analytically to give $e_k(\rho)$; the constant of integration is a reference energy e_0. The Grüneisen parameter was represented using Al'tshuler's asymptotic power law form

$$\Gamma(\rho) = \Gamma_\infty + (\rho_0/\rho)^q(\Gamma_0 - \Gamma_\infty), \tag{A3}$$

which can be integrated analytically to give a volume-dependent Einstein heat capacity. The EOS parameters were adjusted to reproduce pure-phase regions of a tabular multiphase EOS.[40] The α phase was fitted over the range 7.5–8.3 g/cm^3 and 0–800 K, and the ε phase over 8.9–12.3 g/cm^3 and 0–900 K. The cold curve for each phase was fitted well by Heuzé's functional form. The Grüneisen parameter in the α region of the tabular EOS exhibited some temperature dependence, which was not captured by the Grüneisen EOS form; an average value was used. The volume dependence of the Grüneisen parameter was reproduced well by the Al'tshuler form of $\Gamma(\rho)$. The Grüneisen parameter in the ε region of the tabular EOS was independent of temperature, and its volume dependence was again reproduced well by the Al'tshuler form, with $\Gamma_\infty = 0$. The variation of specific heat capacity with temperature and compression in the tabular EOS was reproduced well using the analytic EOS, except at temperatures approaching absolute zero, where the Einstein heat capacity differs significantly from the more physical Debye behavior used to construct the tabular EOS. The parameters used in the phase transformation model are listed in Table I.

For use in studies of the time- and space-dependent response of Fe to dynamic loading, i.e., continuum dynamics simulations, the material was taken to comprise a mixture of phases at each location in the sample, each phase characterized by a volume fraction f_i and a thermodynamic state $\{\rho_i,e_i\}$. Stress and temperature equilibration in the mixture was calculated by altering the f_i and state according to a rapid relaxation rate.[52] Kinetics models were used to describe the rate of conversion of material between phases. The kinetics of the phase transition was treated locally as a function of the difference in free energy, g, between the phases

$$\left.\frac{\partial f_i}{\partial t}\right|_{\to j} = f_i\phi_{ij}[g_i(\rho_i, e_i) - g_j(\rho_j, e_j)]. \tag{A4}$$

The contribution of the elastic strain state can be included in this formalism, though strength was neglected in this initial study. Different forms of the transition rate ϕ were investigated, by comparison with the phase transition feature in the measured velocity histories. For Fe, where the α-ε phase boundary is close to constant in temperature, it was simpler to determine the rate parameters in terms of over-pressurization instead of free energy difference. We found that a fixed time constant for the transition

$$\phi_{ij}(\Delta g) = \frac{\theta(\Delta g)}{\tau}, \tag{A5}$$

where τ is the time constant of the transition and θ the Heaviside step function, reproduced the velocity histories quite poorly. A rate linear in the free energy difference

$$\phi_{ij}(\Delta g) = \alpha\Delta g, \tag{A6}$$

for some constant of proportionality α, was little better. This form is closely related to the rates proposed previously for

TABLE I. Parameters used for Phase transformation Kinetics model. T_{D0} is the Debye temperature at a reference density.

	α-Fe	ε-Fe
ρ_0 (g/cm^3)	7.92406	8.30802
K_0 (GPa)	170.283	160.857
N_0	4.78932	5.56327
e_0 (MJ/kg)	−4.43345	−3.40349
Γ_0	1.66832	2.32805
Γ_∞	0	0
q	0.870667	1.36353
c_{v0} (MJ/kg·K)	540.302×10^{-6}	484.810×10^{-6}
T_{D0} (K)	413.824	322.188

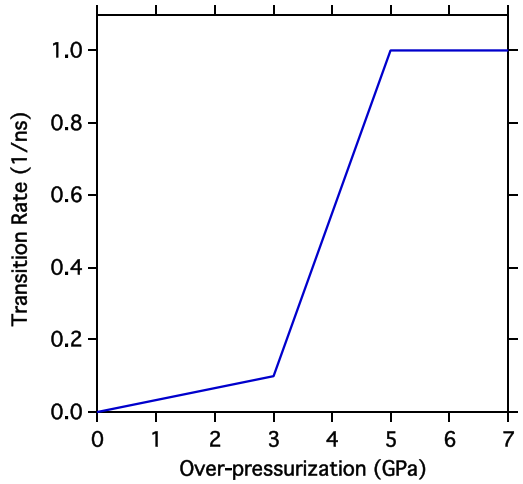

FIG. 10. Fe $\alpha \rightarrow \varepsilon$ phase transformation transition rate versus level of overpressurization of the 12.9 GPa equilibrium phase boundary; as used in the phase transformation kinetics model.

the α-ε transition in Fe.[3,8] A closer match was obtained using a two-stage rate

$$\phi_{ij}(\Delta g) = \alpha(\Delta g)\Delta g = \Delta g[\alpha_1\theta(\Delta g) + \alpha_2\theta(\Delta g - \Delta g_2)], \tag{A7}$$

suggesting that, at the strain rates considered here, a more explicit representation of the nucleation of daughter phase within the parent followed by growth from the nuclei may be needed to capture the response of the material. This observation seems consistent with previous comparisons with velocity histories from ramp-loading on the Z machine.[6] Some improvement was obtained by capping the transition rate to $\sim$1/ns for levels of overpressurization $>$5 GPa, which suggests the onset of a qualitatively different, rate-limiting process such as phonon drag. The final rate used was thus piecewise linear between a sequence of points in pressure beyond the equilibrium transition (Fig. 10).

[1]N. von Bargen and R. Boehler, High Pressure Res. **6**, 133 (1990); R. Boehler, N. von Bargen, and A. Chopelas, J. Geophys. Res. **95**, 21731, doi:10.1029/JB095iB13p21731 (1990); R. D. Taylor, M. P. Pasternak, and R. Jeanloz, J. Appl. Phys. **69**, 6126 (1991).
[2]D. Bancroft, E. L. Peterson, and S. Minshall, J. Appl. Phys. **27**, 291 (1956).
[3]L. M. Barker and R. E. Hollenbach, J. Appl. Phys. **45**, 4872 (1974); L. M. Barker, *ibid.* **46**, 2544 (1975).
[4]B. J. Jensen, G. T. Gray III, and R. S. Hixson, J. Appl. Phys. **105**, 103502 (2009).
[5]J. W. Forbes and G. E. Duvall, in *Proceedings of the Forth International Conference on High Pressure, Kyoto*, edited by J. Osugi (The Physico-Chemical Society of Japan, Kyoto, 1974), p. 480.
[6]M. Bastea, S. Bastea, and R. Becker, Appl. Phys. Lett. **95**, 241911 (2009).
[7]D. H. Kalantar, J. F. Belak, G. W. Collins, J. D. Colvin, H. M. Davis, J. H. Eggert, T. C. Germann, J. Hawreliak, B. L. Holian, K. Kadau, P. S. Lomdahl, H. E. Lorenzana, M. A. Meyers, K. Rosolankova, M. S. Schneider, J. Sheppard, J. S. Stolken, and J. S. Wark, Phys. Rev. Letts. **95**, 075502 (2005).
[8]J. C. Boettger and D. C. Wallace, Phys. Rev. B **55**, 2840 (1997).
[9]K. Kandu, T. C. Germann, P. S. Lomdahl, and B. L. Holian, Phys. Rev. B **72**, 064120 (2005).
[10]J. Hawreliak, J. D. Colvin, J. H. Eggert, D. H. Kalantar, H. E. Lorenzana, J. S. Stölken, H. M. Davies, T. C. Germann, B. L. Holian, K. Kadau, P. S. Lomdahl, A. Higginbotham, K. Rosolankova, J. Sheppard, and J. S. Wark, Phys. Rev. B **74**, 184107 (2006); J. A. Hawreliak, D. H. Kalantar, J. S. Stölken, B. A. Remington, and H. E. Lorenzana, *ibid.* **78**, 220101 (2008).
[11]P. G. Debenedetti, Nature **441**, 168 (2006).
[12]M. Grujicic and G. B. Olson, Interf. Sci. **6**, 155 (1998).
[13]R. F. Smith, J. H. Eggert, M. D. Saculla, A. F. Jankowski, M. Bastea, D. G. Hicks, and G. W. Collins, Phys. Rev. Lett. **101**, 065701 (2008).
[14]C. A. Hall, Phys. Plasmas **7**, 2069 (2000).
[15]The Janus Laser is located in the Lawrence Livermore National Laboratory (LLNL), CA, USA.
[16]The Omega Laser is located in the Laboratory for Laser Energetics (LLE), University of Rochester, NY, USA.
[17]J. H. Eggert, M. Bastea, D. B. Reisman, S. Rothman, J.-P. Davis, M. D. Knudson, D. B. Hayes, G. T. Gray III, D. Erskine, and G. W. Collins, AIP Conf. Proc. **955**, 1177 (2007).
[18]J. Wang, R. F. Smith, J. H. Eggert, D. Braun, T. R. Boehly, J. R. Patterson, P. M. Celliers, R. Jeanloz, G. W. Collins, and T. S. Duffy, J. Appl. Phys. **114**, 023513 (2013).
[19]P. M. Celliers, D. K. Bradley, G. W. Collins, D. G. Hicks, T. R. Boehly, and W. J. Armstrong, Rev. Sci. Instrum. **75**, 4916 (2004).
[20]J.-P. Davis, J. Appl. Phys. **99**, 103512 (2006).
[21]W. F. Hemsing, Rev. Sci. Instrum. **50**, 73 (1979); D. H. Dolan, Sandia Rep., SAND2006-1950 (2006).
[22]R. F. Smith, J. H. Eggert, A. Jankowski, P. M. Celliers, M. J. Edwards, Y. M. Gupta, J. R. Asay, and G. W. Collins, Phys. Rev. Lett. **98**, 065701 (2007).
[23]J. R. Maw, AIP Conf. Proc. **706**, 1217 (2004); S. D. Rothman *et al.*, J. Phys. D **38**, 733 (2005).
[24]W. Arnold, *Dynamisches Werkstoffverhalten von Armco-Eisen bei Stosswellenbelastung* (VDI-Verlag, Duesseldorf, 1992).
[25]*LASL Shock Hugoniot Data*, edited by S. P. Marsh (Univ. California Press, Berkeley, 1980).
[26]R. G. McQueen, J. W. Marsh, J. W. Taylor, J. N. Fritz, and W. J. Carter, in *High Velocity Impact Phenomena*, edited by R. Kinslow (Academic Press, New York, 1970), pp. 515–568; R. G. McQueen and S. P. Marsh, J. Appl. Phys. **31**, 1253 (1960).
[27]J. M. Walsh, M. H. Rice, R. G. McQueen, and F. L. Yarger, Phys. Rev. **108**, 196 (1957).
[28]J. M. Brown and R. G. McQueen, J. Geophys. Res. **91**, 7485, doi:10.1029/JB091iB07p07485 (1986).
[29]A. Dewaele, P. Loubeyre, F. Occelli, M. Mezouar, P. I. Dorogokupets, and M. Torrent, Phys. Rev. Lett. **97**, 215504 (2006).
[30]R. F. Smith, R. W. Minich, R. E. Rudd, J. H. Eggert, C. A. Bolme, S. L. Brygoo, A. M. Jones, and G. W. Collins, Phys. Rev. B **86**, 245204 (2012).
[31]B. J. Jensen, P. A. Rigg, M. D. Knudson, R. S. Hixson, G. T. Gray III, B. H. Sencer, and F. J. Cherne, AIP Conf. Proc. **845**, 232 (2006).
[32]O. V. Fat'yanov, R. L. Webb, and Y. M. Gupta, J. Appl. Phys. **97**, 123529 (2005).
[33]R. F. Smith, J. H. Eggert, R. E. Rudd, D. C. Swift, C. A. Bolme, and G. W. Collins, J. Appl. Phys. **110**, 123515 (2011).
[34]P. L. Héreil, J. Phys. Colloq. C **3**, 77 (1988).
[35]J. C. Crowhurst, M. R. Armstrong, K. B. Knight, J. M. Zaug, and E. M. Behymer, Phys. Rev. Lett. **107**, 144302 (2011).
[36]B. A. Remington, P. Allen, E. M. Bringa, J. Hawreliak, D. Ho, K. T. Lorenz, H. Lorenzana, J. M. McNaney, M. A. Meyers, S. W. Pollaine, K. Rosolankova, B. Sadik, M. S. Schneider, D. Swift, J. Wark, and B. Yaakobi, Mater. Sci. Technol. **22**, 474 (2006).
[37]R. Becker, A. Arsenlis, G. Hommes, J. Marian, M. Rhee, and L. H. Yang, LLNL-TR-417075 (2009).
[38]J. W. Swegle and D. E. Grady, J. Appl. Phys. **58**, 692 (1985); D. E. Grady, *ibid.* **107**, 013506 (2010).
[39]D. C. Swift, N. D. Drummond, O. Heuzé, R. G. Kraus, and G. J. Ackland, 43rd Lunar and Planetary Science Conference, held March 19–23, 2012 at The Woodlands, Texas. LPI Contribution No. 1659, id.2545 (2012). Available at http://www.lpi.usra.edu/meetings/lpsc2012/pdf/2545.pdf.
[40]G. I. Kerley, Sandia National Laboratories Rep., SAND93-0227 (1993).
[41]J. R. Rygg, J. H. Eggert, J. A. Hawreliak, A. E. Lazicki, F. Coppari, T. M. Uphaus, C. M. Sorce, B. Yaakobi, D. G. Hicks, R. F. Smith, and G. W. Collins, Rev. Sci. Instrum. **83**, 113904 (2012).
[42]N. V. Chandra Shekar and K. Govinda Rajan, Bull. Mater. Sci. **24**, 1 (2001).
[43]J. W. Christian, *The Theory of Transformations in Metals and Alloys* (Pergamon, Oxford, 1965) pp. 11–12, 802.
[44]J. C. Phillips, *Bonds and Bands in Semiconductors* (Academic, New York, 1973), p. 221.

[45]A. C. Pan, T. J. Rappl, D. Chandler, and N. P. Balsara, J. Phys. Chem. B **110**, 3692 (2006).
[46]H. J. Schöpe, G. Bryant, and W. van Megan, Phys. Rev. Lett. **96**, 175701 (2006).
[47]A. K. Singh, Bull. Mater. Sci. **5**, 219 (1983); Mater. Sci. Forum **3**, 291 (1985).
[48]M. D. Knudson and Y. M. Gupta, J. Appl. Phys. **91**, 9561 (2002).
[49]M. Bastea, S. Bastea, J. E. Reaugh, and D. B. Reisman, Phys. Rev. B **75**, 172104 (2007).
[50]O. Heuzé, AIP Conf. Proc. **845**, 212 (2006).
[51]M. Missonnier and O. Heuzé, AIP Conf. Proc. **845**, 262 (2006).
[52]R. N. Mulford and D. C. Swift, AIP Conf. Proc. **620**, 415 (2002).
[53]D. Hebert, I. Bertron, and O. Heuzé, AIP Conf. Proc. **1195**, 1205 (2009).